Crystal structure of the papain-like protease of MERS coronavirus reveals unusual, potentially druggable active-site features

CrossMark

Jian Lei [a,c], Jeroen R. Mesters [a,c], Christian Drosten [b,c], Stefan Anemüller [a,c], Qingjun Ma [a,c], Rolf Hilgenfeld [a,c,*]

[a] Institute of Biochemistry, Center for Structural and Cell Biology in Medicine, University of Lübeck, Ratzeburger Allee 160, 23538 Lübeck, Germany
[b] Institute of Virology, University of Bonn Medical School, 53127 Bonn, Germany
[c] German Center for Infection Research (DZIF), Germany

A B S T R A C T

The Middle-East Respiratory Syndrome coronavirus (MERS-CoV) causes severe acute pneumonia and renal failure. The MERS-CoV papain-like protease (PL^{pro}) is a potential target for the development of antiviral drugs. To facilitate these efforts, we determined the three-dimensional structure of the enzyme by X-ray crystallography. The molecule consists of a ubiquitin-like domain and a catalytic core domain. The catalytic domain displays an extended right-hand fold with a zinc ribbon and embraces a solvent-exposed substrate-binding region. The overall structure of the MERS-CoV PL^{pro} is similar to that of the corresponding SARS-CoV enzyme, but the architecture of the oxyanion hole and of the S3 as well as the S5 specificity sites differ from the latter. These differences are the likely reason for reduced *in vitro* peptide hydrolysis and deubiquitinating activities of the MERS-CoV PL^{pro}, compared to the homologous enzyme from the SARS coronavirus. Introduction of a side-chain capable of oxyanion stabilization through the Leu106Trp mutation greatly enhances the *in vitro* catalytic activity of the MERS-CoV PL^{pro}. The unique features observed in the crystal structure of the MERS-CoV PL^{pro} should allow the design of antivirals that would not interfere with host ubiquitin-specific proteases.

© 2014 The Authors. Published by Elsevier B.V. This is an open access article under the CC BY license (http://creativecommons.org/licenses/by/3.0/).

1. Introduction

Ten years after the outbreak of severe acute respiratory syndrome (SARS) of 2002/2003 (Hilgenfeld and Peiris, 2013), another highly pathogenic coronavirus, Middle-East Respiratory Syndrome coronavirus (MERS-CoV), has been recognized to infect humans (Zaki et al., 2012; de Groot et al., 2013). Accumulating evidence suggests camels to act as a zoonotic source of the virus (Reusken et al., 2013; Haagmans et al., 2014; Meyer et al., 2013). Limited human-to-human transmission of the virus has been described (Assiri et al., 2013). As of June 11, 2014, 683 cases of MERS have been reported, with 204 deaths (http://www.who.int). The clinical symptoms of MERS include severe pneumonia and sometimes acute renal failure (Eckerle et al., 2013). However, the majority of MERS patients had/has comorbidities, such as diabetes, lung disease, or chronic renal disease (Perlman, 2013).

SARS-CoV and MERS-CoV belong to the genus *Betacoronavirus* but pertain to highly distinct phylogenetic clades termed b and c, respectively (de Groot et al., 2013). In case of SARS-CoV, the best-characterized potential antiviral drug targets are the two viral proteases, the main protease (M^{pro}, also called 3C-like protease, 3CL^{pro}) (Hilgenfeld and Peiris, 2013; Anand et al., 2003; Yang et al., 2003, 2005; Xu et al., 2005; Lu et al., 2006; Verschueren et al., 2008; Zhu et al., 2011; Kilianski et al., 2013) and the papain-like protease (PL^{pro}) (Hilgenfeld and Peiris, 2013; Kilianski et al., 2013; Barretto et al., 2005; Ratia et al., 2006, 2008; Baez-Santos et al., 2014). The latter enzyme exists in all coronaviruses (Woo et al., 2010) and has been shown to be responsible for releasing non-structural proteins (Nsp) 1, 2, and 3 from the N-terminal part of polyproteins 1a and 1ab. The three cleavage sites contain the sequence motif LXGG↓XX. In addition, the SARS-CoV PL^{pro} has been shown to have deubiquitinating and interferon antagonism activities, thereby interfering with the host innate immune response (Barretto et al., 2005; Lindner et al., 2005; Devaraj et al., 2007; Frieman et al., 2009). Specifically, it can prevent the activation of IRF3 (interferon-regulatory factor 3) and antagonize the NF-κB (nuclear factor κ-light-chain-enhancer of activated B cells) pathway, but the

detailed mechanisms involved are still unclear. Very recently, the MERS-CoV PL[pro] has been reported to also have proteolytic, deubiquitinating, and deISG15ylating activities in HEK293T cells (Yang et al., 2013; Mielech et al., 2014) (ISG15 = interferon-stimulated gene 15); it therefore also acts as an interferon antagonist through blocking the IRF3 pathway. Interestingly, these reports differ in their finding that the interferon-antagonizing activity of the MERS-CoV PL[pro] is either independent of (Yang et al., 2013) or dependent on (Mielech et al., 2014) its proteolytic activity.

In spite of the accumulating knowledge on the essential roles of the coronavirus PL[pro] in virus replication and evasion of the host-cell innate immune response (Devaraj et al., 2007; Frieman et al., 2009; Yang et al., 2013; Mielech et al., 2014; Lindner et al., 2007; Clementz et al., 2010), the three-dimensional structures of only two of these enzymes have been reported so far, i.e., that of the PL[pro] from SARS-CoV (Ratia et al., 2006) and that of the PL1[pro] from Transmissible Gastroenteritis Virus (TGEV) (Wojdyla et al., 2010). Here we present the crystal structure of the MERS-CoV PL[pro] at 2.50 Å resolution, in order to unravel the structural basis of the activities of the enzyme and facilitate structure-based drug design efforts. In addition, we report the *in vitro* hydrolytic activities of the enzyme towards two synthetic peptide substrates and a fluorogenic ubiquitin derivative.

2. Materials and methods

2.1. Recombinant production of MERS-CoV papain-like protease (PL[pro])

The PL[pro] of MERS-CoV (strain 2c EMC/2012; GenBank: AFV09327.1) comprises 320 amino-acid residues, corresponding to Gln1482 – Asp1801 of pp1a, and is part of non-structural protein 3. In the interest of an easy description, we renumber Gln1482 into Gln1 here. A gene coding for the PL[pro] was amplified by the polymerase chain reaction (PCR) using the forward primer 5′-CTAGCTAGC-cagttaacaatcgaagtcttagtg-3′ and the reverse primer 5′-CCGCTCGAGttaatcgctactgtattttttggccggg-3′. The resulting PCR product was digested with restriction enzymes NheI and XhoI for ligation into pET-28a (Novagen). Cloning was designed to include an N-terminal hexahistidine (His$_6$) tag and a thrombin cleavage site. The recombinant plasmid was used to transform *Escherichia coli* strain Tuner (DE3) pLacI (Novagen). Transformed cells were grown at 37 °C overnight in LB medium, supplemented with kanamycin (50 µg/mL) and chloramphenicol (34 µg/mL). The culture was used to inoculate LB medium the day after. When the OD$_{600}$ of the culture reached 0.6–0.8, overexpression of the PL[pro] gene was induced for 20 h with the addition of isopropyl-D-thiogalactoside (IPTG, final concentration 0.5 mM) at 20 °C. Subsequently, the culture was harvested by centrifugation for 30 min at ~7300×g and 4 °C. Cells were resuspended in 30 mL buffer A (20 mM Tris–HCl, 500 mM NaCl, 10 mM imidazole, pH 8.8, 10 mM β-mercaptoethanol (BME)) and lysed by sonication on ice. The lysate was centrifuged for 1 h at ~48,000×g and 4 °C to remove the cell debris. The supernatant was applied to a HisTrap™ nickel column (GE Healthcare) and the His-tagged protein was eluted with buffer B (20 mM Tris–HCl, 500 mM NaCl, 500 mM imidazole, pH 8.8, 10 mM BME) using standard protocols. The target protein was processed overnight by thrombin (Sigma) cleavage at 4 °C to remove the His-tag. Left with six extra residues (GSHMAS) at the N-terminus after this processing step, the PL[pro] was further purified by gel filtration (HiLoad™ 16/60 Superdex 200 column, GE Healthcare) using buffer C (20 mM Tris–HCl, 150 mM NaCl, pH 8.8, 10 mM BME).

2.2. Crystallization and diffraction-data collection

Purified PL[pro] was concentrated to ~11 mg/ml in buffer C. Crystallization was performed at 18 °C by using a Phoenix crystallization robot (Art Robbins) employing the sitting-drop vapor-diffusion method, with mixing 0.25 µl of protein and 0.25 µl of reservoir to equilibrate against 75 µl reservoir solution. The following commercially available screens were used: SaltRx™, PEG/Ion™ 1 & 2 Screen, Index™, and PEG Rx™ 1 & 2 (Hampton Research). Crystals were observed under condition 19 of Index™. Optimized crystals were subsequently obtained within one day using 0.056 M NaH$_2$PO$_4$, 1.344 M K$_2$HPO$_4$, pH 8.0, and 15% glycerol as reservoir, with mixing 2 µl of protein and 2.5 µl of reservoir to equilibrate against 500 µl reservoir solution.

Crystals were flash-cooled in a 100-K nitrogen-gas stream. A dataset to 2.50 Å resolution was collected using synchrotron radiation at wavelength 0.98 Å at beamline P11 of DESY, Hamburg. Diffraction data were processed with the program *XDS* (Kabsch, 2010). The space group was determined as *C2*, with unit-cell parameters a = 100.89 Å, b = 47.67 Å, c = 88.43 Å, β = 122.35°. Diffraction data statistics are given in Table 1.

2.3. Phase determination, model building and refinement

The structure of the MERS-CoV PL[pro] was solved by molecular replacement using the program *BALBES* (Long et al., 2008). The program selected molecule A of the SARS-CoV PL[pro] (PDB: **2FE8**, Ratia et al., 2006) as the most suitable search model. The resulting model for the MERS-CoV PL[pro] was inspected and rebuilt using *Coot* (Emsley et al., 2010), and refined using *autoBUSTER* (Bricogne et al., 2011). The final refinement statistics are presented in Table 1. Atomic coordinates and structure factors have been deposited in the PDB with accession code **4P16**. All figures except Fig. 3 and

Table 1
Data collection and refinement statistics.

	MERS-CoV PL[pro]
Data collection statistics	
Space group	C2
Unit-cell dimensions (Å, °)	a = 100.89, b = 47.67, c = 88.43
	β = 122.35
Wavelength (Å)	0.98
V_m (Å^3/Da)	2.53
Solvent content (%)	51.34
Resolution range (Å)	42.62–2.50 (2.64–2.50)
Number of unique reflections	12337
R_{merge}	0.059 (0.472)
R_{pim}[1]	0.025 (0.194)
Completeness (%)	99.0 (98.3)
Mean I/σ (I)	19.2 (3.9)
Multiplicity	6.6 (6.8)
Refinement statistics	
R_{cryst} (%)[2]	18.7 (23.6)
R_{free} (%)[2]	23.4 (30.3)
No. of atoms	
Protein	2462
Ligand/ion	1
Water	94
Clashscore[3]	2
r.m.s.deviation in bond lengths (Å)	0.01
r.m.s.deviation in bond angles (°)	1.13
Average *B*-factor for all atoms (Å^2)	61
Ramachandran plot	
Residues in favored regions (%)	96.8
Residues in additionally allowed regions (%)	3.2
Residues in outlier regions (%)	0

[1] R_{pim} (Weiss and Hilgenfeld, 1997).
[2] $R_{cryst} = \sum_{hkl}|F_o(hkl) - F_c(hkl)|/\sum_{hkl} F_o(hkl)$. R_{free} was calculated for a test set of reflections (4.9%) omitted from the refinement.
[3] Clashscore is defined as the number of clashes calculated for the model per 1000 atoms (including hydrogens) of the model. Hydrogens were added by *MolProbity* (Chen et al., 2010).

Supplementary Fig. 1 have been prepared using *Pymol* (Schrödinger; http://www.pymol.org/).

2.4. Site-directed mutagenesis

Using the pET28a-PL^pro plasmid as template, site-directed mutagenesis (L106W mutation) was performed by PCR with the following primers (mutated codons shown in bold and underlined): gtacgttctctcaaa**tgg**agtgataataat and acaattattatcact**cca**tttgagagaacg. The PCR products were digested by DpnI (Thermo Scientific) and transformed to DH5α directly. The positive clones were incubated in LB medium overnight and the bacterial culture was harvested next day. The plasmids were purified from the bacteria using the GeneJET Plasmid Miniprep Kit (Thermo Scientific). All DNA plasmids were sequenced and the correctness of the mutation was verified. The procedures for the expression of the construct carrying the L106W mutation and the purification of the corresponding protein were the same as described above for the wild-type protein.

2.5. Assays of MERS-CoV PL^pro in vitro activity

Before usage of the freshly prepared MERS-CoV PL^pro for determination of the enzyme kinetics, the number of free (non-oxidized) cysteine residues was determined by titration with Ellman's reagent (Riddles et al., 1983). All procedures followed the standard protocol of the Ellman's Reagent kit (Thermo Scientific). The resulting number of 13.4 ± 0.3 free cysteine residues (out of 13 in the amino-acid sequence) showed that in the bulk of our enzyme preparation, the catalytic Cys111 was in the free state and fully reduced.

We also examined the influence of ethylene diamine tetraacetic acid (EDTA) on the enzyme's activity, but found no effect of concentrations up to 10 mM. However, at a concentration of 20 mM, a decrease of enzymatic activity was observed, presumably due to the removal of Zn^{2+} from the PL^pro zinc finger. Accordingly, the kinetic assays were carried out in the absence of EDTA.

All enzymatic assays were performed in 20 mM Tris–HCl, 150 mM NaCl, pH 7.9, 2 mM dithiothreitol (DTT), using a 96-well microtiter plate. Three fluorogenic substrates, Cbz-Arg-Leu-Arg-Gly-Gly-7-amino-4-methylcoumarin (Z-RLRGG-AMC) (Bachem), Z-LRGG-AMC and ubiquitin-AMC (Ub-AMC) (BostonBiochem), were used. The enzymatic cleavage reactions were monitored at 25 °C by measuring the increased fluorescence (λ_{ex}: 360 nm; λ_{em}: 460 nm) resulting from AMC release, using an Flx800 fluorescence spectrophotometer (BioTek). Reactions were started by addition of the substrate to the microtiter plate. The kinetic assays were run under the following conditions: 1 μM MERS-CoV PL^pro with different concentrations (10–100 μM) of Z-RLRGG-AMC in a final volume of 100 μl, 1 μM MERS-CoV PL^pro with different concentrations (20–160 μM) of Z-LRGG-AMC in a final volume of 100 μl, or 100 nM PL^pro with different concentrations (0.2–1.2 μM) of Ub-AMC in a final volume of 50 μl. In case of the PL^pro carrying the L106W mutation, the following conditions were used: 125 nM enzyme with different concentrations (10–100 μM) of Z-RLRGG-AMC in a final volume of 100 μl, 250nM enzyme with different concentrations (10–100 μM) of Z-LRGG-AMC in a final volume of 100 μl, or 125 nM PL^pro with different concentrations (0.1–1.0 μM) of Ub-AMC in a final volume of 50 μl. Initial velocities were determined from the linear section of the curve. Since no saturation could be observed, the data were fitted to the equation $v/[E]_{tot.} = k_{app}[S]$, where k_{app} approximates k_{cat}/K_M, as described in Barretto et al. (2005) and Wojdyla et al. (2010). A calibration curve was generated by measuring the fluorescence of free AMC in reaction buffer at concentrations ranging from 0.005 μM to 2.5 μM.

3. Results and discussion

3.1. Overall structure of MERS-CoV PL^pro

The MERS-CoV PL^pro molecule is divided into two parts, the N-terminal ubiquitin-like (Ubl) domain and the catalytic domain (Fig. 1A). The Ubl domain consists of the 62 N-terminal amino-acid residues. It comprises five β-strands, one α-helix, and one 3_{10}-helix (η) in the order β1-β2-α1-β3-β4-η1-β5. The catalytic domain forms an extended right-hand scaffold, which comprises three distinct subdomains: thumb, fingers, and palm. The thumb domain consists of six α-helices and four β-strands with the order α2-α3-β6-β7-α4-β8-α5-α6-α7-β9. The fingers domain contains β10–β13, the N-terminal 16 residues (Glu231–Leu246) of β14, η2, α8, and the C-terminal 7 residues (Phe312–Ser318) of β19. It also includes a zinc finger, in which four cysteine residues (Cys191, Cys194, Cys226, and Cys228) coordinate a zinc ion (Fig. 1A and B). The palm domain comprises six β-strands: β15–β18, the C-terminal 10 residues (Ser247–Thr256) of β14, and the N-terminal 10 residues (Asp302–Leu311) of β19. In the loop Gly271-Gly277 between β15 and β16, residues Ile272–Ala275 are not defined by electron density, indicative of high flexibility. The substrate-binding site is a solvent-exposed region between the palm and thumb
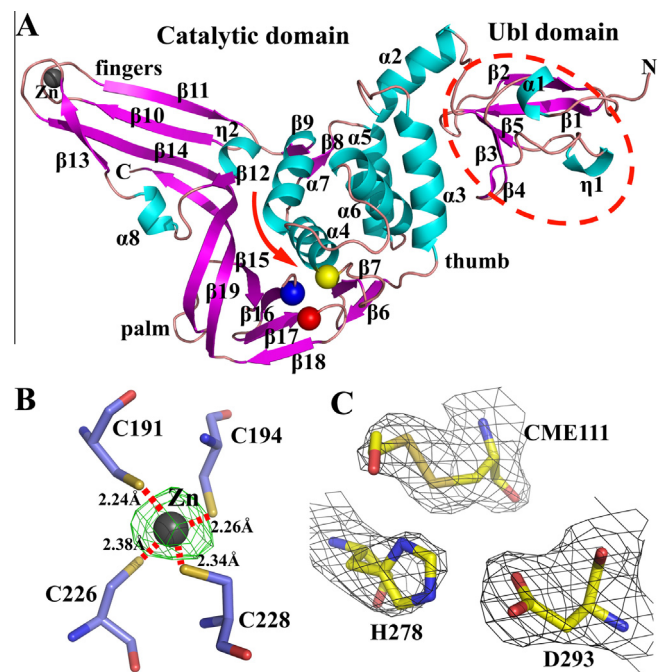

Fig. 1. Structure of the MERS-CoV papain-like protease (PL^pro). (A) Cartoon view of the enzyme's overall structure. α-Helices (cyan) and β-strands (purple) are numbered, polypeptide segments devoid of repetitive secondary structure, including loops and turns, are brown. The ubiquitin-like (Ubl) domain is encircled by a red dashed line. The catalytic domain consists of the thumb, fingers, and palm subdomains. The structural zinc ion in the fingers domain is indicated by a gray sphere. The Cα atoms of the catalytic-site cysteine (111), histidine (278), and aspartate (293) residues are also shown (yellow, blue, and red sphere, respectively). The red arrow indicates the substrate-binding region and points to the catalytic site. (B) The four cysteine ligands (Cys191, Cys194, C226 and C228) and the structural zinc ion (gray sphere) in the zinc ribbon of the fingers domain. An F_o-F_c omit density (green; contoured at 5 σ above the mean) for the zinc is shown. Sulfur atoms are shown in yellow, oxygen in red, nitrogen in blue, and carbon in light blue. The coordinative bonds between the sulfur atoms and the zinc ion are indicated by dashed red lines. (C) The catalytic triad: Cys111, His278, and Asp293. Atom colors: carbon, yellow; oxygen, red; nitrogen, blue. A $2F_o$-F_c electron density (gray; contoured at 1.0 σ above the mean) is also displayed. CME111: Cys111 covalently modified by β-mercaptoethanol.

domains (Fig. 1A and C). At the center of this region, the catalytic triad consisting of Cys111, His278, and Asp293 is located (Fig. 1C).

Interestingly, the segment 283-RLKGG↓Li-289, located in the connection between the active-site residues His278 and Asp293, constitutes a potential autocleavage site for the MERS-CoV PL^pro. Whereas we have some preliminary evidence for partial autoprocessing of our protease preparation at this site (data not shown), the electron density maps suggest that no cleavage has occurred in the crystallized protein at this position. Residues 283–285 are at the C-terminus of strand β16 and the two glycines are the central residues of a β-turn that leads into strand β17, which starts with Leu288. Thus, the residues concerned are part of well-defined secondary-structure elements and therefore, although largely accessible to solvent, cannot be accommodated by the substrate-binding site of the protease. However, whether or not in-trans PL^pro autocleavage occurs at this position in the viral polyprotein, remains to be investigated.

3.2. Comparisons of the overall fold

3.2.1. The Ubl domain

As the Ubl domain and the catalytic domain of the MERS-CoV PL^pro are two independent domains, we treated them separately in searching the Protein Data Bank (PDB) for structural similarity using the DALI server (Holm and Rosenström, 2010). However, we note that there are no variations in the relative orientation of these domains with respect to each other, as the Ubl domain is anchored to the core domain by two strong salt-bridges in MERS-CoV PL^pro (Arg16...Glu64, 2.9 Å; Asp39...His81, 3.5 Å) as well as in SARS-CoV PL^pro (the TGEV PL1^pro lacks the Ubl domain). The structural comparisons show that the MERS-CoV Ubl domain is similar to other proteins or domains featuring the ubiquitin fold (Table 2, Fig. 2A). The Ubl domain of SARS-CoV PL^pro is essential for downregulating IRF3 or the NF-κB antiviral signaling pathway, but the Ubl domain alone is not sufficient to do so (Frieman et al., 2009). On the other hand, the Ubl domain is often involved in protein–protein interactions (Mueller and Feigon, 2003; Su and Lau, 2009; Hartmann-Petersen and Gordon, 2004) and it is conceivable that the Ubl domain of MERS-CoV PL^pro could interfere with host signaling-pathway proteins by providing a binding scaffold, which is necessary for the catalytic domain to accomplish its function of antagonizing the host's innate immune response.

3.2.2. The catalytic domain: comparison with other coronaviral PL^pros

The catalytic domain of the MERS-CoV PL^pro is more similar to that of the SARS-CoV (Ratia et al., 2006) than to the PL1^pro of
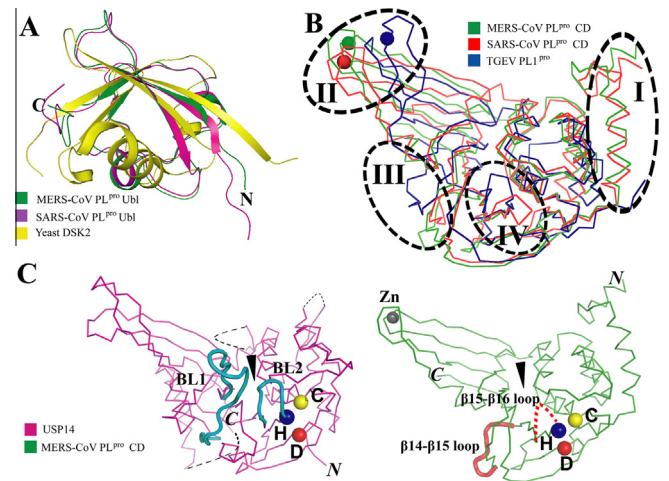

Fig. 2. Comparison of the MERS-CoV PL^pro with other coronavirus PL^pros and human ubiquitin-specific protease 14 (USP14). (A) Superposition of the MERS-CoV PL^pro Ubl domain (green) with the SARS-CoV PL^pro Ubl domain (purple, PDB: 2FE8, chain A, Ratia et al., 2006) and yeast DSK2 (yellow, PDB: 2BWF, chain B, Lowe et al., 2006). All three adopt the globular β-grasp fold. The N and C termini of the MERS-CoV PL^pro Ubl domain are marked. (B) Superposition of the catalytic domain (CD) of MERS-CoV PL^pro (green) with the SARS-CoV PL^pro CD (red, PDB: 2FE8, chain A, Ratia et al., 2006) and with TGEV PL1^pro (blue, PDB: 3MP2, Wojdyla et al., 2010). Four regions of structural differences are apparent (encircled by dashed black lines and labeled with roman numbers). The structural zinc ion in the fingers domain of each protease is indicated by a green, red, and blue sphere, respectively. (C) Side-by-side comparison of USP14 (left, purple, PDB: 2AYN, chain B, Hu et al., 2005) and MERS-CoV PL^pro CD (right, green). The Cα positions (yellow, blue, and red sphere, respectively) of the catalytic-triad cysteine, histidine, and aspartate residues are shown for each protease. The two "blocking loops", BL1 and BL2, of USP14 are highlighted in cyan. The loop β14-β15 (salmon) of MERS-CoV, which corresponds to BL1 of USP14, is oriented towards the opposite direction in the PL^pro. The dashed red line indicates the loop β15-β16 in MERS-CoV PL^pro (corresponding to BL2 of USP14) that was not defined by electron density in our structure. The dashed black lines indicate disordered regions in USP14. The structural zinc ion of MERS-CoV PL^pro is indicated by a gray sphere. The black arrow indicates the substrate binding region of each protease. The N and C termini of each enzyme are marked with letters in italics.

Transmissible Gastroenteritis Virus (TGEV; Wojdyla et al., 2010) (Table 2). There are four regions of significant structural difference between the coronaviral PL^pros (Fig. 2B). The first (Region I) concerns the two helices α2 and α3 in the N-terminal region of the thumb domain of the MERS-CoV and SARS-CoV enzymes, which are absent in the TGEV PL1^pro (Figs. 2B and 3). The second region (II in Fig. 2B) of

Table 2
Structural comparisons of MERS-CoV PL^pro with other proteins.

	MERS-CoV PL^pro ubiquitin-like (Ubl) domain					
	PDB/chain ID	Z score	RMSD (Å)	Cα[1]	% id[2]	References
SARS-CoV PL^pro Ubl	**2FE8**/A	11.0	1.1	61/64	28	Ratia et al. (2006)
DSK2	**2BWF**/B	5.5	2.1	54/77	17	Lowe et al. (2006)
hHR23A	**1P98**/A	5.2	2.1	56/78	7	Mueller and Feigon (2003)
	MERS-CoV PL^pro catalytic domain (CD)					
	PDB/chain ID	Z score	RMSD (Å)	Cα[1]	% id[2]	References
SARS-CoV PL^pro CD	**2FE8**/A	27.4	2.4	246/251	32	Ratia et al. (2006)
TGEV PL1^pro	**3MP2**/A	18.7	3.1	198/211	23	Wojdyla et al. (2010)
USP14	**2AYN**/B	13.0	3.1	199/337	14	Hu et al. (2005)
USP21	**3I3T**/A	12.8	3.0	196/303	15	Ernst et al. (2013)
USP2	**2HD5**/A	12.8	3.1	198/315	15	Renatus et al. (2006)
USP7	**1NB8**/B	10.5	3.5	198/333	15	Hu et al. (2002)

[1] Aligned Cα atoms/total Cα atoms.
[2] Sequence identity.

major structural differences concerns the four β-strands of the fingers domain. Two β-hairpins, which provide the cysteine residues for binding the structural zinc ion in this region, are twisted to different degrees among the three structures. The third structurally different area (III in Fig. 2B) is the connecting region between the fingers and palm domains. In the MERS-CoV PL^{pro}, the C-terminal 10 residues of β14 extend into the palm domain and an 8-residue loop (Thr257–Val264) connects β14 and β15. In the SARS-CoV enzyme, the corresponding strand is divided into two separate β-strands, β12 and β13, the latter of which is mostly part of the palm domain, and a shorter loop formed by 5 residues (Gln256 - Leu260) connects β13 and β14. In the TGEV PL1^{pro}, there are two loops (Ser157–Thr160 and Val166–Val170) and one 3$_{10}$-helix (Pro161–Phe165) connecting the fingers and palm domains. The different connections in the various PL^{pro}s might lead to different mutual orientations of the two domains, which in turn might affect the enzymatic activities of the individual PL^{pro}s. Finally, Region IV (Fig. 2B) concerns the loop between β15 and β16 (Gly271–Gly277), four residues of which are not defined by electron density in MERS-CoV PL^{pro}. The corresponding region in TGEV PL1^{pro} (Gly177–Gly182) and in SARS-CoV PL^{pro} (Gly267–Gly272) is shorter by one residue compared to the MERS-CoV enzyme; it forms a loop between β8 and β9 in TGEV PL1^{pro} and a short 3$_{10}$-helix between β14 and β15 in the SARS-CoV enzyme. However, this region is very flexible and adopts different positions in the three copies of the SARS-CoV PL^{pro} in the asymmetric unit of the crystal (Ratia et al., 2006). In the recently reported crystal structure of the SARS-CoV PL^{pro} (C112S mutant) in complex with ubiquitin (Chou et al., 2014), the β14-β15 loop shows large conformational differences compared to its position in the free enzyme. The two glycines framing this loop are absolutely conserved among the coronavirus PL^{pro}s, but the residues between them are different in each of the enzymes, suggesting that there must be differences in the interaction between the loop and the substrates.

3.2.3. Comparison with cellular ubiquitin-specific proteases

Even though the catalytic domain of the MERS-CoV PL^{pro} only shares 12–15% sequence identity with the cellular ubiquitin-specific proteases (USPs), it features largely the same fold as the USPs with known three-dimensional structures (Table 2). A side-by-side comparison of the catalytic domain of the MERS-CoV PL^{pro} with USP14 is shown in Fig. 2C. The most significant differences are located in the connecting region between the fingers and palm domains. The two "blocking loops", BL1 and BL2, of USP14 regulate the deubiquitinating activity (Hu et al., 2005) (Fig. 2C). BL1 of USP14 connects the fingers and palm domains. It is a 22-residue loop between β8 and β9, exposed to the substrate-binding surface. The corresponding loop in MERS-CoV PL^{pro} is much shorter (8 residues) and connects β14 and β15. Furthermore, this short loop does not face the substrate-binding region but rather points to the bottom of the thumb domain of MERS-CoV PL^{pro} (Fig. 2C), and can thus not be considered a "blocking loop". As a consequence, the substrate-binding site (indicated by the black arrow in Fig. 2C) is larger in MERS-CoV PL^{pro} than in the USPs, probably enabling the enzyme to not only bind ubiquitin but also viral polyprotein. Connecting β10 and β11, the other blocking loop, BL2 (residues Gly427–Gly433), of USP14 is near the active site and undergoes conformational change upon substrate binding (Hu et al., 2005); this loop corresponds to β15-β16 (residues Gly271–Gly277) of MERS-CoV PL^{pro} which unfortunately lacks electron density for four of its seven residues (see above).

3.3. The active site of MERS-CoV PL^{pro}

The MERS-CoV PL^{pro} possesses a catalytic triad consisting of Cys111, His278, and Asp293 (Figs. 1C and 4A). Cys111 in the MERS-CoV PL^{pro} is situated at the N-terminus of α4 and points into the substrate-binding cleft between the palm and thumb domains.
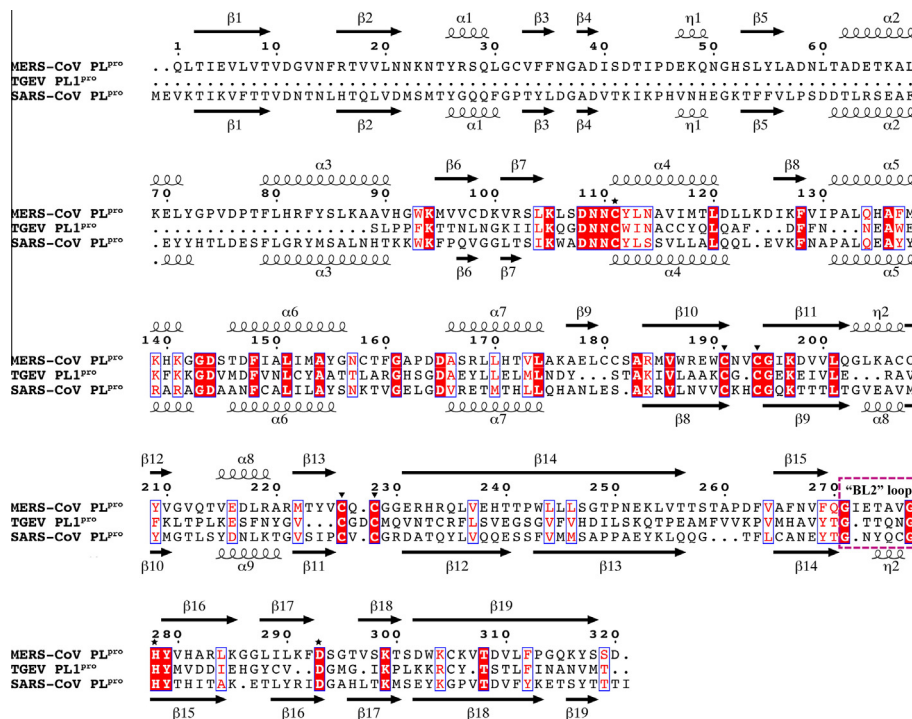

Fig. 3. Structure-based alignment of MERS-CoV PL^{pro} (GenBank: AFV09327.1), SARS-CoV PL^{pro} (GenBank: AY278741.1), and TGEV PL1^{pro} (GenBank: AJ271965.2). Secondary-structure elements of MERS-CoV PL^{pro} (top) and SARS-CoV PL^{pro} (bottom) are indicated. Residues of the catalytic triad are marked by black asterisks. The four cysteine residues coordinating the zinc ion are marked by black inverted triangles. The mobile β 15–β 16 loop (corresponding to BL2 of USP14) is indicated by a dashed purple box. Residues that are identical in the three CoV proteases are marked by white letters in red boxes with blue outline, while similar residues are marked by red letters and a blue outline. The figure was created by using the program ESPript (Gouet et al., 1999).

There is clear electron density indicating that the catalytic cysteine has been modified by disulfide bond formation with β-mercap-toethanol (BME) during crystallization of the enzyme. His278 is located at the N-terminus of β16; its Nδ1 atom is 4.4 Å from the
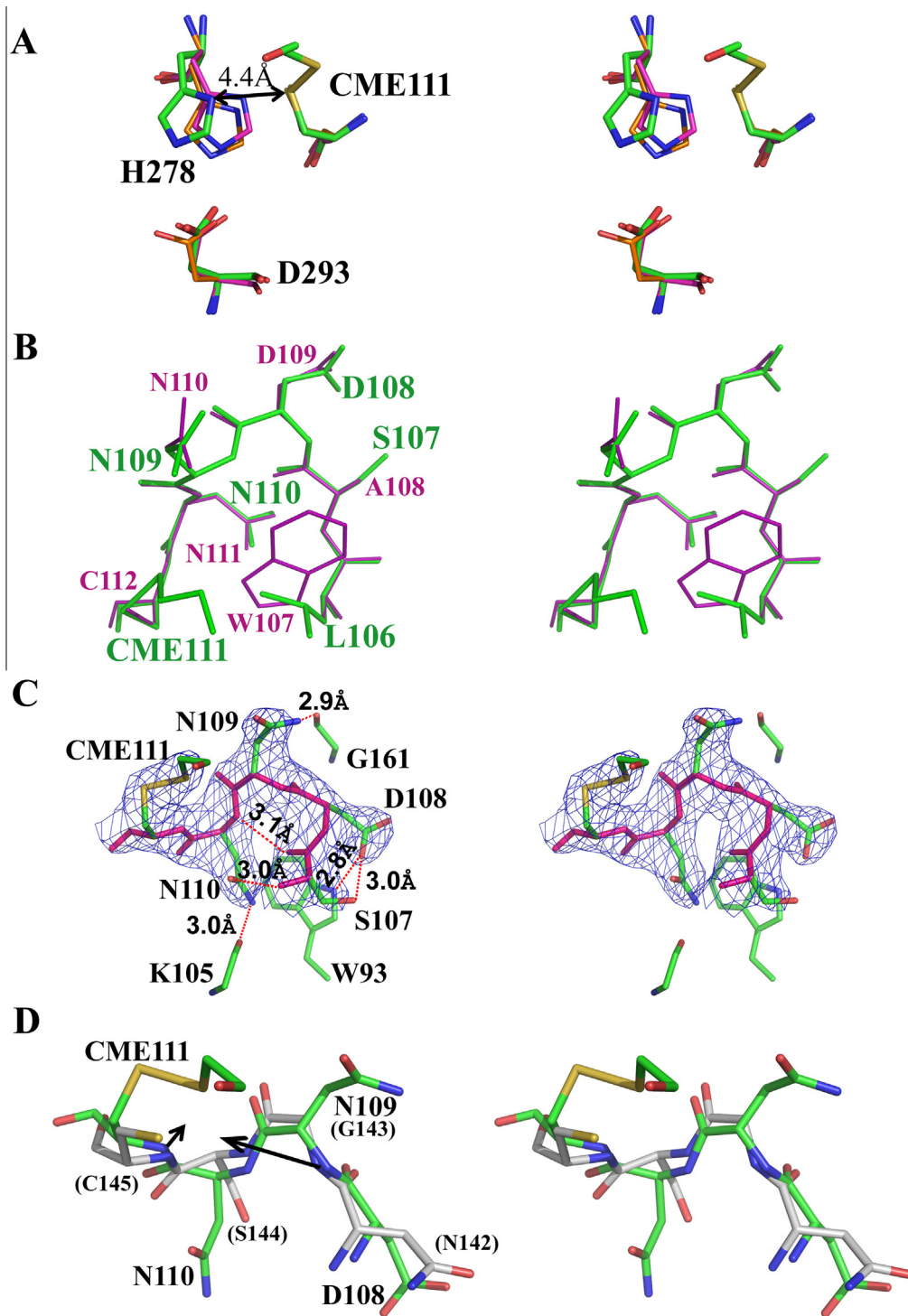

Fig. 4. Active site of MERS-CoV PL^{pro}. (A) Superposition (stereo view) of catalytic-triad residues of MERS-CoV PL^{pro} (thick green sticks), SARS-CoV PL^{pro} (thin purple sticks, PDB: 2FE8, chain A, Ratia et al., 2006), and USP14 (thin orange sticks, PDB: 2AYN, chain B, Hu et al., 2005). The distance between Nδ1 of His278 and the sulfur of Cys111 in MERS-CoV PL^{pro} is indicated. CME111: Cys111 covalently modified by β-mercaptoethanol. (B) Superposition (stereo view) of the polypeptide segment preceding the catalytic cysteine in MERS-CoV PL^{pro} (106-LSDNN(CME)-111, green, shown as thick sticks, with bold green labels) and SARS-CoV PL^{pro} (107-WADNNC-112, purple, thin sticks, smaller purple labels). (C) Stereo view of the same β-turn, Ser107-Asp108-Asn109-Asn110, in MERS-CoV PL^{pro}, with the corresponding 2F$_o$-F$_c$ electron density (blue; contoured at 1.5 σ above the mean). The main chain of the β-turn and of the (modified) catalytic residue CME111 is shown in pink, while side-chains are green. Gly161, Lys105 (main chain), and Trp93 (side-chain) are displayed as well. Hydrogen bonds are indicated by dashed red lines. (D) Stereo view of a superposition of 108-DNN(CME)-111 in MERS-CoV PL^{pro} (green) and 142-NGSC-145 in SARS-CoV M^{pro} (gray, PDB: 2BX3, Tan et al., 2005). Residues of MERS-CoV PL^{pro} and SARS-CoV M^{pro} (in brackets) are labeled. The RMSD of all main-chain atoms between this pair of four residues is ∼0.62 Å. The two black arrows point to the presumable position of the oxyanion in the transition state of the proteolytic reaction.

sulfur of Cys111. This large distance is likely due to the BME-modification of Cys111; in most papain-like protease structures, the distances are between 3.7 Å and 4.0 Å (Fig. 4A). Although the side-chain of His278 is somewhat displaced from its regular position in the catalytic triad, Asp293 and Cys111 align well with their counterparts in SARS-CoV PL^pro and USP14 (Fig. 4A).

The transition state of the proteolytic reaction catalyzed by papain-like cysteine proteases is stabilized in the oxyanion hole, through two hydrogen bonds usually donated by the main-chain amide of the catalytic cysteine residue and by the side-chain amide of a glutamine or asparagine residue five or six positions N-terminal to the catalytic cysteine. For example, the latter residue is Asn in USP14 and HAUSP (Hu et al., 2002, 2005), and Gln in the ubiquitin C-terminal hydrolases (UCH)-L3 and UCH-L1 (Johnston et al., 1997). In TGEV PL1^pro, there is also a glutamine residue (Gln27) at this position (Wojdyla et al., 2010). In SARS-CoV PL^pro, the corresponding residue is Trp107, the indole NH of which has been proposed to stabilize the oxyanion transition state (Fig. 4B). Accordingly, replacing Trp by Ala abrogates the protease activity (Ratia et al., 2006). Surprisingly, the corresponding residue in the MERS-CoV PL^pro is Leu106, the side-chain of which is incapable of hydrogen bonding (Fig. 4B).

How then is the oxyanion transition state stabilized in MERS-CoV PL^pro? Ratia et al. (2006) have discussed Asn110 as a potential additional component of the oxyanion hole in the SARS-CoV PL^pro. This residue is highly conserved amongst the coronaviral PL^pros, including the MERS-CoV enzyme (Asn109) and in TGEV PL1^pro (Asn30). In all three coronavirus PL^pros of known three-dimensional structure as well as in USP14, this Asn residue occupies position i+2 of a β-turn (Ser107-Asp108-Asn109-Asn110 in MERS-CoV) that precedes the catalytic cysteine in the polypeptide chain. However, the side-chain of Asn109 is oriented away from the oxyanion hole and is involved in a strong (2.9 Å) hydrogen-bond with the carbonyl oxygen of conserved Gly161 of the thumb subdomain (Fig. 4C); therefore, it is unlikely to undergo a conformational change that will bring it into the neighborhood of the catalytic center. The other two potential hydrogen-bonding donors in this β-turn, Ser107 and Asn110, are heavily engaged in hydrogen bonds across the turn (Fig. 4C) and therefore equally unlikely to undergo the conformational changes necessary to reorient their side-chains towards the catalytic center.

So if none of the side-chains in this β-turn is a likely component of the oxyanion hole, what about main-chain amides? We notice that the segment between residues 108 (position i+1 of the β-turn) and 111 can be superimposed (with an RMSD of ~0.62 Å for main-chain atoms) onto the loop (142-NGSC-145) preceding the catalytic nucleophile, Cys145, in SARS-CoV main protease (M^pro; PDB: **2BX3**, Tan et al., 2005) (Fig. 4D). The M^pro is a cysteine protease comprising a chymotrypsin-like fold; in these enzymes, the oxyanion hole is formed by the main-chain amides of the catalytic cysteine (or serine) and of the penultimate residue (Taranto et al., 2008; Wu et al., 2013). The penultimate residue before the catalytic nucleophile in chymotrypsin-like proteases is absolutely conserved as a glycine, whereas in MERS-CoV PL^pro, the conserved Asn109 resides at this position. However, this asparagine is in a left-handed (α_L) conformation, with positive ϕ and ψ angles (56° and 34°, resp.) in the Ramachandran plot, just like the conserved glycine in the catalytically competent conformation of chymotrypsin-like proteases (Verschueren et al., 2008; Tan et al., 2005). In fact, Asn and Asp are the only residues apart from Gly, for which this conformation is observed at a significant rate in protein structures (Hutchinson and Thornton, 1994). (Incidentally, in MERS-CoV PL^pro, the i+1 residue of this β-turn, Asp108, is also in an α_L conformation, so that we have the rare situation here of a β-turn with both i+1 and i+2 residues having positive ϕ/ψ angles). In spite of the Asn109 main-chain N

atom being relatively well superimposable onto the corresponding atom of Gly143 in SARS-CoV M^pro, we note that the N-H vector of this amide does not point towards the position that would likely be assumed by the oxyanion. Whether or not the necessary (minor) rearrangement may occur, remains to be answered by elucidating the structure of a complex between the MERS-CoV PL^pro and a transition-state analogue.

In any case, our mutation experiment described below clearly demonstrates that the oxyanion hole of the MERS-CoV PL^pro is deficient.

3.4. The substrate-binding site of MERS-CoV PL^pro

In the MERS-CoV polyproteins, the three cleavage sites for the PL^pro are KLIGG↓DV (Nsp1-2), RLKGG↓AP (Nsp2-3), and KIVGG↓AP (Nsp3-4). The P1 and P2 positions are strictly conserved as glycine residues. P5 is Lys or Arg and P4 Leu or Ile, whereas P3 can be Ile, Lys, or Val. In the SARS-CoV polyprotein, cleavage by the PL^pro also occurs behind LXGG, but X is either Asn or Lys (Barretto et al., 2005), never a hydrophobic residue such as Ile or Val as in MERS-CoV. The LXGG motif is also present at the C-terminus of ubiquitin. In addition to the crystal structure of the complex between the C112S mutant of SARS-CoV PL^pro and ubiquitin (Chou et al., 2014), the structure of the wild-type SARS-CoV PL^pro with Ubal has very recently been reported (Ratia et al., 2014; Ubal is ubiquitin with the C-terminal carboxylate reduced to an aldehyde, which forms a covalent bond with the catalytic Cys residue). However, as the PDB coordinates for the latter structure have not been released yet, we rely for our further discussion on the structures of the ubiquitin complex of the SARS-CoV PL^pro (C112S mutant) and on the structure of USP14-Ubal; Hu et al., 2005). The structural homology between these two enzymes and MERS-CoV PL^pro allowed us to deduce conclusions concerning the substrate-binding site of the latter. When we superimposed the substrate-binding sites of MERS-CoV PL^pro, SARS-CoV PL^pro(C112S), and USP14, we found a remarkable degree of structural conservation but also some important differences (Fig. 5).

In MERS-CoV PL^pro, the substrate-binding site is lined by residues Leu106–Tyr112 and Gly161–Arg168 of the thumb subdomain, and Phe269–Tyr279, Pro250, and Thr308 of the palm subdomain (Fig. 5C and D). Asn109, Cys111, the NH of Tyr112, Gly277, and His278 (all conserved in SARS-CoV PL^pro and USP14) form the spatially restricted S1 site (Fig. 5C and D), which can only accommodate glycine as the P1 residue. Pro163 (Leu163 in SARS-CoV PL^pro, Gln196 in USP14), Asp164 (main chain), Gly277 (conserved), and Tyr279 (side-chain, conserved) are involved in shaping the equally restricted S2 subsite, which again is specific for glycine (Fig. 5C and D). Replacement of Tyr274 in SARS-CoV PL^pro (corresponding to Tyr279 of the MERS-CoV enzyme) by Ala leads to a loss of protease activity (Barretto et al., 2005).

The S3 subsite of MERS-CoV PL^pro features important differences from the one in the SARS-CoV enzyme. In the SARS-CoV PL^pro(C112S)-Ub and SARS-CoV PL^pro-Ubal complexes (Chou et al., 2014; Ratia et al., 2014), the main-chain amide of *P3-Arg* (substrate residues are indicated in italics in what follows) forms an H-bond with the side-chain OH of Tyr265 (Fig. 5A and S1A). In MERS-CoV PL^pro, this residue is replaced by Phe269 (Fig. 5C and D). Replacement of Tyr265 by Phe in SARS-CoV PL^pro reduces the peptidolytic activity of the enzyme by a factor of 2.4 and its deubiquitinating activity by 57% (Chou et al., 2014). Another potentially important difference between the S3 subsites of SARS-CoV PL^pro and MERS-CoV PL^pro is that Glu162 of the former is replaced by Ala162 in the latter (Fig. 5A and C), reducing the negative electrostatic potential of this region in the MERS-CoV PL^pro (Fig. 5E and F). This might enable the MERS-CoV enzyme to accommodate hydrophobic P3
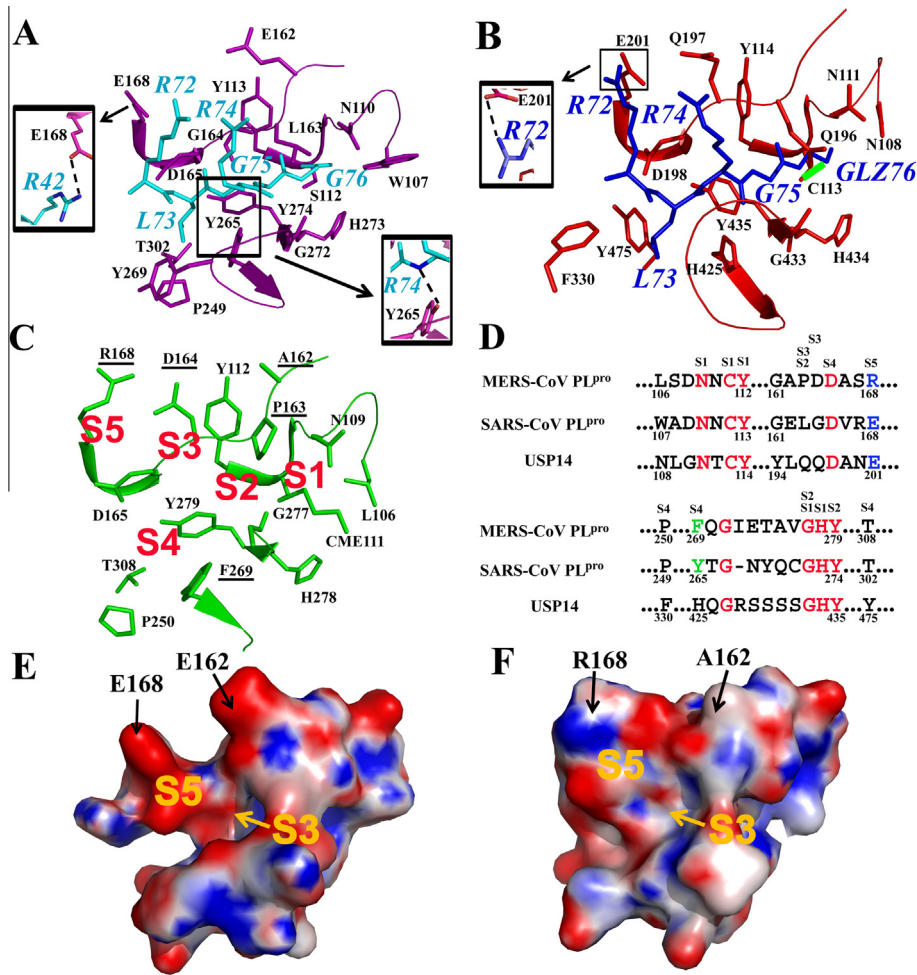
Fig. 5. Substrate-binding site of MERS-CoV PL^{pro} as deduced from the homologous structures of SARS-CoV PL^{pro} and USP14. (A) The substrate-binding site in SARS-CoV PL^{pro} (purple, PDB: 4M0W (complex with ubiquitin), Chou et al., 2014). The five C-terminal residues of ubiquitin, RLRGG, are displayed as cyan sticks. Ubiquitin residues are labeled by cyan letters in *italics*, and residues of SARS-CoV PL^{pro} involved in binding the C-terminal residues of ubiquitin are labeled with black regular letters. The salt-bridge Glu168...*Arg42* and the hydrogen bond Tyr265...*Arg74* are highlighted in insets. (B) The substrate-binding site of USP14 (red, PDB: 2AYO, complex with ubiquitin-aldehyde, Hu et al., 2005). The five C-terminal residues of ubiquitin, RLRGG-aldehyde, in the complex are displayed as blue sticks (GLZ, amino-acetaldehyde, i.e. the aldehyde of the C-terminal *G76*). The P1-P5 residues of ubiquitin are labeled by blue letters in *italics*. Residues of USP14 involved in binding the C-terminal residues of ubiquitin are labeled with regular black letters. The covalent bond between sulfur (Cys113) and carbon (*GLZ76*) is displayed by a green line. The salt-bridge Glu201...*Arg72* is highlighted in the inset. (C) The substrate-binding site of MERS-CoV PL^{pro}. Residues that are different from those of SARS-CoV PL^{pro} and USP14 are underlined. The supposed positions of the subsites S1–S5 are indicated. (D) Structure-based alignment of residues involved in defining specificity subsites in MERS-CoV PL^{pro}, SARS-CoV PL^{pro}, and USP14. Conserved residues are in red. Arg168 of MERS-CoV PL^{pro} (corresponding to Glu168 and Glu201 in SARS-CoV PL^{pro} and USP14, respectively) is in blue. Phe269 of the MERS-CoV enzyme (Tyr265 in SARS-CoV PL^{pro}) is green. Residues involved in shaping subsites are labeled by the symbol for the corresponding subsite (S1–S5) above the alignment. Residues contributing to S1, S2, and S4, but not S3 and S5, are conserved. (E, F) Electrostatic surfaces of the substrate-binding regions of SARS-CoV PL^{pro} (E) and MERS-CoV PL^{pro} (F), colored according to electrostatic potential (blue, positive potential; red, negative potential). The electrostatic surfaces were calculated using the APBS plugin in PyMOL (Baker et al., 2001). The contouring level is -8 k_BT/e to 8 k_BT/e. Orientation is the same as in the cartoon representations in (A and C). The S3 and S5 subsites are indicated by orange labels. (E) Glu162 and Glu168 of SARS-CoV PL^{pro} are marked. (F) Ala162 and R168 of MERS-CoV PL^{pro} are marked.

residues such as Ile or Val, as they occur at the PL^{pro} cleavage sites of the MERS-CoV (but not the SARS-CoV) polyprotein.

The S4 subsite in MERS-CoV PL^{pro} is a hydrophobic pocket formed by Thr308, Pro250, Phe269, and the Cβ atom of conserved Asp165. The side-chain carboxylate of the latter may interact with the amide of *P4-Leu*. Accordingly, replacement of this aspartate by Ala in SARS-CoV PL^{pro} inactivates the enzyme (Chou et al., 2014). Phe269 is involved in both the S3 subsite (see above) and in making hydrophobic interactions with the *P4-Leu* of polyprotein cleavage sites or ubiquitin. In addition, the mobile β 15–β 16 loop probably contributes to the S4 site (as deduced from the structure of SARS-CoV PL^{pro} in complex with ubiquitin (Chou et al., 2014)), but we are unable to provide a detailed description because of missing electron density (see above). In any case, however, the loop of the MERS-CoV enzyme is devoid of a large aromatic residue

that could make interactions with *Leu73 (P4)* (and *Leu71 (P6)*) of ubiquitin, as observed for Tyr269 of SARS-CoV PL^{pro} (Chou et al., 2014).

Table 3
Kinetic parameters of MERS-CoV PL^{pro}.

	Z-RLRGG-AMC	Z-LRGG-AMC	Ub-AMC
MERS-CoV PL^{pro}			
WT[#]	1.31 ± 0.14[*]	1.00 ± 0.01	$(5.06 ± 0.35) \times 10^2$
L106W	53.27 ± 5.10	60.16 ± 7.00	$(1.70 ± 0.58) \times 10^3$
SARS-CoV PL^{pro}			
WT (Lindner et al., 2005)		∼3.6	∼7.86×10^2
WT (Barretto et al., 2005)			∼4.48×10^3

[#] Wild-type.
[*] k_{app} (min^{-1} mM^{-1}).

The S5 subsite of MERS-CoV PL[pro] is also different from that in USP14 and in the SARS-CoV PL[pro]. The side-chain of the *P5-Arg* forms a salt-bridge with Glu201 in the USP14-Ubal complex (Hu et al., 2005; Fig. 5B and S1B) and the same is observed for Glu168 of SARS-CoV PL[pro] with Ubal (Ratia et al., 2014). However, in the SARS-CoV PL[pro](C112S) complex with ubiquitin (Chou et al., 2014), this same glutamate residue interacts with an arginine of the core of ubiquitin (*Arg42*) instead of the *P5-Arg* (Fig. 5A). This may be due to the position of Glu168 and hence the entire S5 site of the PL[pro] at the surface of the protease, near the entrance to the substrate-binding cleft. While not forming a pocket, the S5 is still important for substrate binding, because the Glu168 side-chain is at the core of a region with pronounced negative electrostatic potential (see Fig. 5E). Interestingly, this important glutamate of USP14 and SARS-CoV PL[pro] is replaced by Arg168 in MERS-CoV PL[pro] (Fig. 5D), changing the electrostatic potential of the S5 site of the latter to more positive and therefore less ideal for interacting with the *P5-Arg* or *Arg42* of ubiquitin, or the *P5 Lys/Arg* of the MERS-CoV polyprotein cleavage sites (Fig. 5F). Indeed, Chou et al. (2014) have replaced Glu168 of SARS-CoV PL[pro] by Arg and found a 25-fold decrease in deubiquitinating activity of the enzyme.

Mesecar and colleagues have demonstrated that the SARS-CoV PL[pro] is a druggable target. They used their crystal structure of the enzyme (Ratia et al., 2006) in a virtual screening campaign and reported crystal structures of the complex with the optimized hit compound, GRL0617 (5-amino-2-methyl-N-[(1R)-1-naphthalen-1-ylethyl]benzamide) and derivatives thereof (Ratia et al., 2008; Baez-Santos et al., 2014). Interestingly, the inhibitors do not bind to the catalytic center directly but near the S3 and S4 subsites as well as the mobile β 14–β 15 loop (β 15–β 16 in MERS-CoV PL[pro]) (Ratia et al., 2008; Baez-Santos et al., 2014). As there are important differences in the S3 subsite as well as in the mobile loop between the SARS-CoV and the MERS-CoV PL[pro]s, it is unlikely that these compounds will inhibit the PL[pro] and the replication of MERS-CoV. However, virtual or real screening approaches might be expected to result in the discovery of different small-molecule compounds binding to a similar site in MERS-CoV PL[pro].

3.5. In-vitro peptide-hydrolysis and deubiquitinating activities of wild-type MERS-CoV PL[pro] and its L106W variant

We tested the PL[pro]-catalyzed hydrolysis of the peptides Z-RLRGG-7-amino-4-methylcoumarin (AMC) and Z-LRGG-AMC as mimics of the cleavage sites in the viral polyproteins. For this assay (and the one described below), only freshly prepared enzyme was used, in which the catalytic cysteine residue was shown to be in a free, reduced (and hence active) state by titration with Ellman's reagent and by the absence of an effect of adding EDTA up to a concentration of 10 mM (see Materials & Methods). We found that the peptides were hydrolyzed by MERS-CoV PL[pro] *in vitro*, and that the initial rate of hydrolysis increased with raising the substrate concentration. However, we were unable to observe saturation of the reactions. This might indicate a large K_m value and/or low enzyme efficiency. We used the pseudo-first-order rate constant, k_{app}, to estimate an approximate k_{cat}/K_m value. The k_{app} rates were 1.31 ± 0.14 min^{-1} mM^{-1} for Z-RLRGG-AMC and 1.00 ± 0.01 min^{-1} mM^{-1} for Z-LRGG-AMC, values significantly lower than those reported for the SARS-CoV PL[pro] (Table 3). This may be explained by the apparent deficiency of the oxyanion hole of the MERS-CoV PL[pro] and the inability of the side-chain of Phe269 to form the hydrogen bond with the main-chain amide of *P3-Arg* observed for the corresponding Tyr265 in SARS-CoV PL[pro] (Chou et al., 2014). In order to examine whether this relatively low activity is caused by the deficiency of the oxyanion hole, i.e. the lack of a side-chain available for oxyanion stabilization through hydrogen bonding, we prepared the L106W mutant of the MERS-CoV PL[pro]

and found its peptide-hydrolyzing activities on Z-RLRGG-AMC and Z-LRGG-AMC, respectively, to be 40-fold and 60-fold higher than those of the wild-type enzyme (Table 3). This is a clear demonstration of the deficiency of the oxyanion hole in the MERS-CoV PL[pro] and shows that the contribution to oxyanion stabilization by the main-chain amide of residue 109, if at all existent, is far less efficient than by a tryptophan residue in position 106, as found in the SARS-CoV PL[pro].

We also tested the deubiquitinating activity of the MERS-CoV PL[pro] *in vitro* using Ub-AMC as a substrate. We determined k_{app} as $(5.06 \pm 0.35) \times 10^2$ min^{-1} mM^{-1}. This value is also lower than the rate constants reported for SARS-CoV PL[pro] by different research groups (Table 3). Again, the less-than-perfect oxyanion hole and the replacement of Tyr265 of SARS-CoV PL[pro] by Phe269 in MERS-CoV PL[pro] may be responsible for this. In addition, the replacement of Glu168 of SARS-CoV PL[pro] by Arg168 in the MERS-CoV enzyme very likely weakens the interaction with ubiquitin. The deubiquitinating activity of the MERS-CoV PL[pro] carrying the L106W mutation was found to be 3.4-fold higher than that of the wild-type enzyme (Table 3). Our results demonstrate that the MERS-CoV PL[pro] displays both peptidase and deubiquitinase activities *in vitro* and is thus suitable for screening chemical libraries for inhibitors.

4. Conclusions

The crystal structure of the MERS-CoV PL[pro] provides critical information on this important potential drug target. The unique architecture of the oxyanion hole, which differs from all papain-like proteases that have been structurally characterized so far, may be of fundamental interest. Because of unique features of its S3 and S5 subsites as well as in the flexible loop (β 15–β 16) covering the substrate-binding site, we expect that the MERS-CoV PL[pro] will show differences in ubiquitin recognition, compared to SARS-CoV PL[pro] and USP14. Both peptidase and deubiquitinating activities of MERS-CoV PL[pro] have been demonstrated *in vitro*. Introduction of the L106W mutation leads to a restoration of the oxyanion hole of the PL[pro] and an enhancement of both catalytic activities. Furthermore, the structural differences from homologous host enzymes such as USP14 should allow the design of antivirals devoid of too many side effects.

Appendix A. Supplementary data

Supplementary data associated with this article can be found, in the online version, at http://dx.doi.org/10.1016/j.antiviral.2014.06.011.

References

Anand, K., Ziebuhr, J., Wadhwani, P., Mesters, J.R., Hilgenfeld, R., 2003. Coronavirus main proteinase (3CL[pro]) structure: basis for design of anti-SARS drugs. Science 300, 1763–1767.

Assiri, A., McGeer, A., Perl, T.M., Price, C.S., Al Rabeeah, A.A., Cummings, D.A., Alabdullatif, Z.N., Assad, M., Almulhim, A., Makhdoom, H., Madani, H., Alhakeem, R., Al-Tawfiq, J.A., Cotton, M., Watson, S.J., Kellam, P., Zumla, A.I., Memish, Z.A., KSA MERS-CoV Investigation Team, 2013. Hospital outbreak of Middle East respiratory syndrome coronavirus. N. Engl. J. Med. 369, 407–416.

Baez-Santos, Y.M., Barraza, S.J., Wilson, M.W., Agius, M., Mielech, A.M., Davis, N.M., Baker, S.C., Larsen, S.D., Mesecar, A.D., 2014. X-ray structural and biological evaluation of a series of potent and highly selective inhibitors of human coronavirus papain-like proteases. J. Med. Chem. 57, 2393–2412. http://dx.doi.org/10.1021/jm401712t.

Baker, N.A., Sept, D., Joseph, S., Holst, M.J., McCammon, J.A., 2001. Electrostatics of nanosystems: application to microtubules and the ribosome. Proc. Natl. Acad. Sci. U.S.A. 98, 10037–10041.

Barretto, N., Jukneliene, D., Ratia, K., Chen, Z., Mesecar, A.D., Baker, S.C., 2005. The papain-like protease of severe acute respiratory syndrome coronavirus has deubiquitinating activity. J. Virol. 79, 15189–15198.

Bricogne, G., Blanc, E., Brandl, M., Flensburg, C., Keller, P., Paciorek, W., Roversi, P., Sharff, A., Smart, O.S., Vonrhein, C., Womack, T.O., 2011. BUSTER Version 2.11.4. Global Phasing Ltd, Cambridge, United Kingdom.

Chen, V.B., Arendall, W.B.I.I.I., Headd, J.J., Keedy, D.A., Immormino, R.M., Kapral, G.J., Murray, L.W., Richardson, J.S., Richardson, D.C., 2010. MolProbity: all-atom structure validation for macromolecular crystallography. Acta Crystallogr. D Biol. Crystallogr. 66, 12–21.

Chou, C.Y., Lai, H.Y., Chen, H.Y., Cheng, S.C., Cheng, K.W., Chou, Y.W., 2014. Structural basis for catalysis and ubiquitin recognition by the severe acute respiratory syndrome coronavirus papain-like protease. Acta Crystallogr. D Biol. Crystallogr. 70, 572–581.

Clementz, M.A., Chen, Z., Banach, B.S., Wang, Y., Sun, L., Ratia, K., Baez-Santos, Y.M., Wang, J., Takayama, J., Ghosh, A.K., Li, K., Mesecar, A.D., Baker, S.C., 2010. Deubiquitinating and interferon antagonism activities of coronavirus papain-like proteases. J. Virol. 84, 4619–4629.

de Groot, R.J., Baker, S.C., Baric, R.S., Brown, C.S., Drosten, C., Enjuanes, L., Fouchier, R.A., Galiano, M., Gorbalenya, A.E., Memish, Z.A., Perlman, S., Poon, L.L., Snijder, E.J., Stephens, G.M., Woo, P.C., Zaki, A.M., Zambon, M., Ziebuhr, J., 2013. Middle East respiratory syndrome coronavirus (MERS-CoV): announcement of the coronavirus study group. J. Virol. 87, 7790–7792.

Devaraj, S.G., Wang, N., Chen, Z., Chen, Z., Tseng, M., Barretto, N., Lin, R., Peters, C.J., Tseng, C.T., Baker, S.C., Li, K., 2007. Regulation of IRF-3-dependent innate immunity by the papain-like protease domain of the severe acute respiratory syndrome coronavirus. J. Biol. Chem. 282, 32208–32221.

Eckerle, I., Müller, M.A., Kallies, S., Gotthardt, D.N., Drosten, C., 2013. In-vitro renal epithelial cell infection reveals a viral kidney tropism as a potential mechanism for acute renal failure during Middle East Respiratory Syndrome (MERS) coronavirus infection. Virol. J. 10, 359.

Emsley, P., Lohkamp, B., Scott, W.G., Cowtan, K., 2010. Features and development of Coot. Acta Crystallogr. D Biol. Crystallogr. 66, 486–501.

Ernst, A., Avvakumov, G., Tong, J., Fan, Y., Zhao, Y., Alberts, P., Persaud, A., Walker, J.R., Neculai, A.M., Neculai, D., Vorobyov, A., Garg, P., Beatty, L., Chan, P.K., Juang, Y.C., Landry, M.C., Yeh, C., Zeqiraj, E., Karamboulas, K., Allali-Hassani, A., Vedadi, M., Tyers, M., Moffat, J., Sicheri, F., Pelletier, L., Durocher, D., Raught, B., Rotin, D., Yang, J., Moran, M.F., Dhe-Paganon, S., Sidhu, S.S., 2013. A strategy for modulation of enzymes in the ubiquitin system. Science 339, 590–595.

Frieman, M., Ratia, K., Johnston, R.E., Mesecar, A.D., Baric, R.S., 2009. Severe acute respiratory syndrome coronavirus papain-like protease ubiquitin-like domain and catalytic domain regulate antagonism of IRF3 and NF-kappaB signaling. J. Virol. 83, 6689–6705.

Gouet, P., Courcelle, E., Stuart, D.I., Metoz, F., 1999. ESPript: multiple sequence alignments in PostScript. Bioinformatics 15, 305–308.

Haagmans, B.L., Al Dhahiry, S.H., Reusken, C.B., Raj, V.S., Galiano, M., Myers, R., Godeke, G.J., Jonges, M., Farag, E., Diab, A., Ghobashy, H., Alhajri, F., Al-Thani, M., Al-Marri, S.A., Al Romaihi, H.E., Al Khal, A., Bermingham, A., Osterhaus, A.D., Alhajri, M.M., Koopmans, M.P., 2014. Middle East respiratory syndrome coronavirus in dromedary camels: an outbreak investigation. Lancet Infect. Dis. 14, 140–145.

Hartmann-Petersen, R., Gordon, C., 2004. Integral UBL domain proteins: a family of proteasome interacting proteins. Semin. Cell Dev. Biol. 15, 247–259.

Hilgenfeld, R., Peiris, M., 2013. From SARS to MERS: 10 years of research on highly pathogenic human coronaviruses. Antiviral Res. 100, 286–295.

Holm, L., Rosenström, P., 2010. Dali server: conservation mapping in 3D. Nucleic Acids Res. 38, W545–W549.

Hu, M., Li, P., Li, M., Li, W., Yao, T., Wu, J.W., Gu, W., Cohen, R.E., Shi, Y., 2002. Crystal structure of a UBP-family deubiquitinating enzyme in isolation and in complex with ubiquitin aldehyde. Cell 111, 1041–1054.

Hu, M., Li, P., Song, L., Jeffrey, P.D., Chenova, T.A., Wilkinson, K.D., Cohen, R.E., Shi, Y., 2005. Structure and mechanisms of the proteasome-associated deubiquitinating enzyme USP14. EMBO J. 24, 3747–3756.

Hutchinson, E.G., Thornton, J.M., 1994. A revised set of potentials for beta-turn formation in proteins. Protein Sci. 3, 2207–2216.

Johnston, S.C., Larsen, C.N., Cook, W.J., Wilkinson, K.D., Hill, C.P., 1997. Crystal structure of a deubiquitinating enzyme (human UCH-L3) at 1.8 Å resolution. EMBO J. 16, 3787–3796.

Kabsch, W., 2010. XDS. Acta Crystallogr. D Biol. Crystallogr. 66, 125–132.

Kilianski, A., Mielech, A.M., Deng, X., Baker, S.C., 2013. Assessing activity and inhibition of Middle East respiratory syndrome coronavirus papain-like and 3C-like proteases using luciferase-based biosensors. J. Virol. 87, 11955–11962.

Lindner, H.A., Fotouhi-Ardakani, N., Lytvyn, V., Lachance, P., Sulea, T., Ménard, R., 2005. The papain-like protease from the severe acute respiratory syndrome coronavirus is a deubiquitinating enzyme. J. Virol. 79, 15199–15208.

Lindner, H.A., Lytvyn, V., Qi, H., Lachance, P., Ziomek, E., Ménard, R., 2007. Selectivity in ISG15 and ubiquitin recognition by the SARS coronavirus papain-like protease. Arch. Biochem. Biophys. 466, 8–14.

Long, F., Vagin, A.A., Young, P., Murshudov, G.N., 2008. BALBES: a molecular-replacement pipeline. Acta Crystallogr. D Biol. Crystallogr. 64, 125–132.

Lowe, E.D., Hasan, N., Trempe, J.F., Fonso, L., Noble, M.E., Endicott, J.A., Johnson, L.N., Brown, N.R., 2006. Structures of the Dsk2 UBL and UBA domains and their complex. Acta Crystallogr. D Biol. Crystallogr. 62, 177–188.

Lu, I.L., Mahindroo, N., Liang, P.H., Peng, Y.H., Kuo, C.J., Tsai, K.C., Hsieh, H.P., Chao, Y.S., Wu, S.Y., 2006. Structure-based drug design and structural biology study of novel nonpeptide inhibitors of severe acute respiratory syndrome coronavirus main protease. J. Med. Chem. 49, 5154–5161.

Meyer, B., Müller, M.A., Corman, V.M., Reusken, C.B., Ritz, D., Godeke, G.J., Lattwein, E., Kallies, S., Siemens, A., van Beek, J., Drexler, J.F., Muth, D., Bosch, B.J., Wernery, U., Koopmans, M.P., Wernery, R., Drosten, C., 2013. Antibodies against MERS coronavirus in dromedary camels, United Arab Emirates, 2003 and 2013. Emerg. Infect. Dis. http://dx.doi.org/10.3201/eid2004.131746.

Mielech, A.M., Kilianski, A., Baez-Santos, Y.M., Mesecar, A.D., Baker, S.C., 2014. MERS-CoV papain-like protease has delSGylating and deubiquitinating activities. Virology 450–451, 64–70.

Mueller, T.D., Feigon, J., 2003. Structural determinants for the binding of ubiquitin-like domains to the proteasome. EMBO J. 22, 4634–4645.

Perlman, S., 2013. The Middle East respiratory syndrome – how worried should we be? mBio 4, e00531-13.

Ratia, K., Saikatendu, K.S., Santarsiero, B.D., Barretto, N., Baker, S.C., Stevens, R.C., Mesecar, A.D., 2006. Severe acute respiratory syndrome coronavirus papain-like protease: structure of a viral deubiquitinating enzyme. Proc. Natl. Acad. Sci. U.S.A. 103, 5717–5722.

Ratia, K., Pegan, S., Takayama, J., Sleeman, K., Coughlin, M., Baliji, S., Chaudhuri, R., Fu, W., Prabhakar, B.S., Johnson, M.E., Baker, S.C., Ghosh, A.K., Mesecar, A.D., 2008. A noncovalent class of papain-like protease/deubiquitinase inhibitors blocks SARS virus replication. Proc. Natl. Acad. Sci. U.S.A. 105, 16119–16124.

Ratia, K., Kilianski, A., Baez-Santos, Y.M., Baker, S.C., Mesecar, A., 2014. Structural basis for the ubiquitin-linkage specificity and deISGylating activity of SARS-CoV papain-like protease. PLoS Pathog. 10, e1004113.

Renatus, M., Parrado, S.G., D'Arcy, A., Eidhoff, U., Gerhartz, B., Hassiepen, U., Pierrat, B., Riedl, R., Vinzenz, D., Worpenberg, S., Kroemer, M., 2006. Structural basis of ubiquitin recognition by the deubiquitinating protease USP2. Structure 14, 1293–1302.

Reusken, C.B., Haagmans, B.L., Müller, M.A., Gutierrez, C., Godeke, G.J., Meyer, B., Muth, D., Raj, V.S., Smits-De, Vries.L., Corman, V.M., Drexler, J.F., Smits, S.L., El Tahir, Y.E., De Sousa, R., van Beek, J., Nowotny, N., van Maanen, K., Hidalgo-Hermoso, E., Bosch, B.J., Rottier, P., Osterhaus, A., Gortázar-Schmidt, C., Drosten, C., Koopmans, M.P., 2013. Middle East respiratory syndrome coronavirus neutralising serum antibodies in dromedary camels: a comparative serological study. Lancet Infect. Dis. 13, 859–866.

Riddles, P.W., Blakeley, R.L., Zerner, B., 1983. Reassessment of Ellman's reagent. Methods Enzymol. 91, 49–60.

Su, V., Lau, A.F., 2009. Ubiquitin-like and ubiquitin-associated domain proteins: significance in proteasomal degradation. Cell. Mol. Life Sci. 66, 2819–2833.

Tan, J., Verschueren, K.H., Anand, K., Shen, J., Yang, M., Xu, Y., Rao, Z., Bigalke, J., Heisen, B., Mesters, J.R., Chen, K., Shen, X., Jiang, H., Hilgenfeld, R., 2005. pH-dependent conformational flexibility of the SARS-CoV main proteinase (Mpro) dimer: molecular dynamics simulations and multiple X-ray structure analyses. J. Mol. Biol. 354, 25–40.

Taranto, A.G., Carvalho, P., Avery, M.A., 2008. QM/QM studies for Michael reaction in coronavirus main protease (3CLpro). J. Mol. Graph. Model. 27, 275–285.

Verschueren, K.H., Pumpor, K., Anemüller, S., Chen, S., Mesters, J.R., Hilgenfeld, R., 2008. A structural view of the inactivation of the SARS coronavirus main proteinase by benzotriazole esters. Chem. Biol. 15, 597–606.

Weiss, M.S., Hilgenfeld, R., 1997. On the use of the merging R factor as a quality indicator for X-ray data. J. Appl. Cryst. 30, 203–205.

Wojdyla, J.A., Manolaridis, I., van Kasteren, P.B., Kikkert, M., Snijder, E.J., Gorbalenya, A.E., Tucker, P.A., 2010. Papain-like protease 1 from transmissible gastroenteritis virus: crystal structure and enzymatic activity toward viral and cellular substrates. J. Virol. 84, 10063–10073.

Woo, P.C., Huang, Y., Lau, S.K., Yuen, K.Y., 2010. Coronavirus genomics and bioinformatics analysis. Viruses 2, 1804–1820.

Wu, C.G., Cheng, S.C., Chen, S.C., Li, J.Y., Fang, Y.H., Chen, Y.H., Chou, C.Y., 2013. Mechanism for controlling the monomer-dimer conversion of SARS coronavirus main protease. Acta Crystallogr. D Biol. Crystallogr. 69, 747–755.

Xu, T., Ooi, A., Lee, H.C., Wilmouth, R., Liu, D.X., Lescar, J., 2005. Structure of the SARS coronavirus main proteinase as an active C₂ crystallographic dimer. Acta Crystallogr. F Struct. Biol. Cryst. Commun. 61, 964–966.

Yang, H., Yang, M., Ding, Y., Liu, Y., Lou, Z., Zhou, Z., Sun, L., Mo, L., Ye, S., Pang, H., Gao, G.F., Anand, K., Bartlam, M., Hilgenfeld, R., Rao, Z., 2003. The crystal structures of severe acute respiratory syndrome virus main protease and its complex with an inhibitor. Proc. Natl. Acad. Sci. U.S.A. 100, 13190–13195.

Yang, H., Xie, W., Xue, X., Yang, K., Ma, J., Liang, W., Zhao, Q., Zhou, Z., Pei, D., Ziebuhr, J., Hilgenfeld, R., Yuen, K.Y., Wong, L., Gao, G., Chen, S., Chen, Z., Ma, D.,

Bartlam, Rao, Z., . Design of wide-spectrum inhibitors targeting coronavirus main protease. PLoS Biol. 3, e324.

Yang, X., Chen, X., Bian, G., Tu, J., Xing, Y., Wang, Y., Chen, Z., 2013. Proteolytic processing, deubiquitinase and interferon antagonist activities of Middle East respiratory syndrome coronavirus papain-like protease. J. Gen. Virol. 95, 614–626.

Zaki, A.M., van Boheemen, S., Bestebroer, T.M., Osterhaus, A.D., Fouchier, R.A., 2012. Isolation of a novel coronavirus from a man with pneumonia in Saudi Arabia. N. Engl. J. Med. 367, 1814–1820.

Zhu, L., George, S., Schmidt, M.F., Al-Gharabli, S.I., Rademann, J., Hilgenfeld, R., 2011. Peptide aldehyde inhibitors challenge the substrate specificity of the SARS-coronavirus main protease. Antiviral Res. 92, 204–212.